IET Inspec

Inspec Analytics

Uncover deeper insights into the impact of global research

Understand your place in the global engineering research landscape and make strategic decisions about the direction of your projects with a dynamic research intelligence tool based on the IET's renowned Inspec database.

Precision analytics for research excellence

Enhanced features allow you to uncover deeper insights into the impact of global research and explore the elements most valuable to you. With Inspec Analytics, you can:

–Deepen your understanding of global scientific trends.

–Define the scope of research initiatives to maximise your impact.

–Assess your organisation's research output and impact.

–Evaluate the success of collaborative partnerships.

Learn more at **inspec-analytics.theiet.org**

Received: 6 December 2020 | Revised: 16 April 2021 | Accepted: 4 July 2021

IET Power Electronics

DOI: 10.1049/pel2.12170

The Institution of Engineering and Technology WILEY

ORIGINAL RESEARCH PAPER

An enhanced feedforward flux weakening control for high-speed permanent magnet machine drive applications

Xiaoyu Lang | **Tao Yang** | **Chen Li** | **Seang Shen Yeoh** | **Serhiy Bozhko** | **Patrick Wheeler**

Power Electronics, Machines and Control (PEMC) Group, The University of Nottingham, Nottingham, United Kingdom

Correspondence
Dr. Tao Yang, Room B107a, Coates Building, University Park, Nottingham, NG7 2RD, UK.
Email: tao.yang@nottingham.ac.uk

Funding information
Cleansky, Grant/Award Number: 807081

Abstract

Permanent magnet machines have been used in the high-speed drive applications due to their high-efficiency, high-power-density, and wide-speed range characteristics. However, control of such high-speed permanent magnet machines machine is always challenging and proper flux-weakening controller design is essential to achieve high performance of these machines. In this paper, an improved feedforward flux-weakening control scheme for interior permanent magnet synchronous machine (IPMSM) drives are proposed. The proposed method identifies optimal *d*-axis and *q*-axis currents under different operation regions using maximum-torque-per-ampere curve, voltage limit, and current limit curves with a fast Newton–Raphson algorithm. To ensure the optimal performance of the control mechanism, effects of inductance variations due to the magnetic saturation are considered and an innovative high-frequency staircase voltage injection method is used to identify the *q*-axis inductance. The experimental results show that compared with other existing flux-weakening methods, the proposed technique can improve the DC-link voltage utilisation without the need to tune any controller gains and can fully utilise maximum available torque with desirable transient performance.

1 | INTRODUCTION

In recent years, the interior permanent-magnet synchronous machines (IPMSMs) are widely used in the high-speed drive applications such as electric vehicles [1, 2] due to promising features, including high torque-to-ampere ratio, small volume, fast dynamic response, and most importantly, the geometrically buried magnets of IPMSM's rotor which makes it mechanically robust to operate at a high speed [3, 4]. IPMSMs with a wide constant power to speed ratio are also considered as a potential candidate for the other high-speed applications such as aircraft starter/generator (SG) [5]. The applications of IPMSM for high-speed drive require the machines to operate in a wide speed range (for example, for the aircraft SG the speed ratio is 4:1 to 6:1 range [6]). Different control strategies are expected at different speed range. Generally, below the base speed, the maximum torque per ampere (MTPA) control is preferred to minimise the copper loss in IPMSM. While in the high-speed region, flux-weakening (FW) control should be adopted to realise constant power characteristics [7].

During the past decades, many literatures have been devoted to the FW control of electrical machine drives. In general, the solutions fall into two categories: (1) feedback methods; and (2) feedforward methods. The feedback methods, e.g. [8–11], use an outer voltage loop to automatically identify the onset of the FW control and generate a negative *d*-axis current to prevent the saturation of current controllers at the high speed range (i.e. beyond the base speed). A general diagram of an IPMSM drive system with feedback FW approach is shown in Figure 1.

Typically, the output of the speed regulator is the current magnitude I_s or the torque reference T_e^{ref}. When the voltage magnitude is less than V_{max}, the feedback FW is inactive, i.e. $\Delta i_{dFW} = 0$. The output of speed controller I_s (or T_e^{ref}) is decomposed into *dq*-axes current references on the MTPA curve. Beyond the base speed, a negative Δi_{dFW} will be generated from the FW controller and added to i_{d0}^{ref}, resulting a

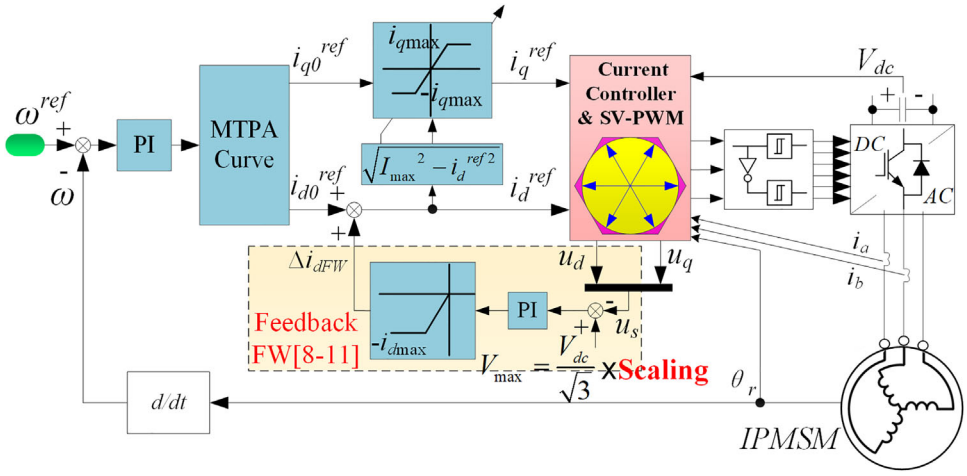

FIGURE 1 Typical block diagram of IPMSM drive system with feedback FW approach

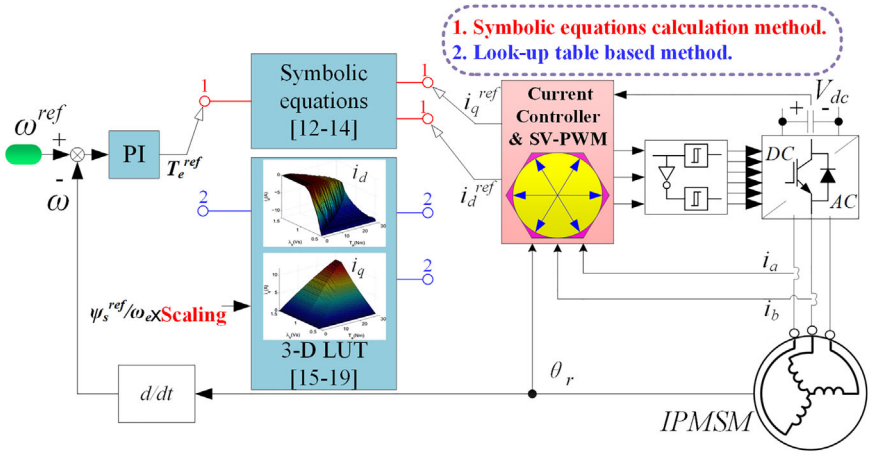

FIGURE 2 Block diagram of IPMSM drive system with feedforward FW approaches

decreased i_d current reference i_d^{ref}. The maximum q-axis current reference is determined by i_d^{ref} and the maximum current allowed $I_{\max}$. Such feedback FW control method ensures that the output power increase beyond the base speed. Another advantage of this method is its independence from parameter variations and only the proportional and integral (PI) gains of the outer voltage control loop need to be tuned.

Although easy for implementation, the feedback FW control method can hardly offer a desirable dynamic performance. The design of the PI parameters of the outer voltage loop is not straightforward as the drive system operates in a voltage saturation region [12]. The design of FW controller is typically achieved using trial and error method. The entire system may operate in an unstable region if the PI parameters are not appropriately tuned.

In contrast to the feedback methods, feedforward methods can provide desirable dynamic performance and guarantee the stability of the drive system. However, the performances of feedforward FW methods are highly dependent on the accuracy of machine parameters. The feedforward FW schemes can be further divided into two categories: (1) "symbolic equations calculation" methods and (2) "look-up table based" schemes. The control block diagram with feedforward FW methods is shown in Figure 2.

The "symbolic equations calculation" methods use the symbolic equations of physical constraints to directly compute the dq-axes current references [13]. Although easy for implementation, those works neglected the influence of stator resistance. However, this assumption is not reasonable when the IPMSM has relatively high stator resistances [14]. In [12], the influences of stator resistance and its voltage drop are considered by a partial linearisation. But this method depends on the start and end points of the linearised chord. Variations of stator inductances also need to be considered due to the magnetic saturation in IPMSM. Although in [14] both stator resistance and inductance variation are considered, and an optimal control are given based on the symbolic equations, the assumption that q-axis inductance is linear only to q-axis current is oversimplified.

For the "look-up table (LUT) based" feedforward FW schemes, the general idea is to create two 3D tables based on machine parameters and DC bus voltages. The outputs of such tables are dq-axes current references in an entire operating region of IPMSM. In [15, 16], torque reference T_e^{ref} and angular frequency ω_e serve as two searching indexes of the 3D

tables. Optimal currents references with different T_e^{ref} and ω_e are derived using convex optimisation of machine equations. Some other works, such as [17–19], adopt torque reference T_e^{ref} and stator flux linkage reference ψ_s^{ref} as the searching indexes. Using ψ_s^{ref} instead of ω_e is better because the saturation of voltage can be reflected more accurately. In [18, 19], ψ_s^{ref} is obtained from the quotient of DC voltage and speed, and it is compensated by the difference of modulation index. Offline measured machine parameters are required. Though the LUT based feedforward method can reduce the computation time, its performance highly relies on the accuracy of two 3D tables. Moreover, those methods require additional stator flux observers and large memory space for the two tables.

To retain the merits and address the drawbacks of aforementioned methods, an improved feedforward FW scheme considering variations of stator resistance and inductance is proposed in this paper. Here are the four main contributions:

1. Deriving full operating trajectories in constant torque and constant power regions for the studied IPMSM with the proposed feedforward method considering stator resistance and the variation of stator inductance.
2. Using Newton–Raphson algorithm to compute the optimal *dq*-axes current references online.
3. Proposing a new torque limitation method for the proposed FW method dealing with high speed heavy load conditions.
4. Proposing a high-frequency (HF) staircase signal injection method to identify the stator inductance instead of using the conventional sinusoidal signals. The injected signal considers both current loop bandwidth and sampling frequency of digital controller. The nonlinearities of power converter are considered and compensated in the control algorithm. The proposed signal along with the nonlinearity compensation guarantees the accuracy of the stator inductance identification.

The rest of this paper is organised as follows. In Section 2, the feedforward FW scheme is introduced. A new torque limitation method in high speed heavy load conditions is studied in this section. In Section 3, the HF signal injection method for inductance identification is discussed. Section 4 verifies the effectiveness of proposed feedforward FW scheme through experiments on a 2.54 kW IPMSM platform followed by the conclusion in Section 5. The proof of convergence of Newton–Raphson algorithm is exhibited in Appendix.

2 | FLUX WEAKENING CONTROL CONSIDERING STATOR RESISTANCE AND THE VARIATION OF STATOR INDUCTANCE

2.1 | Basics of IPMSM operation

The IPMSM considered in this paper consists of a stator with three-phase windings (one per phase) and a rotor with buried permanent magnets. The stator windings are distributed windings with phase shift of 120°. The state-space voltage equations in the rotor reference frame can be given as:

$$\begin{cases} u_d = R_s i_d + \dfrac{d\psi_d}{dt} - \omega_e \psi_q \\ u_q = R_s i_q + \dfrac{d\psi_q}{dt} + \omega_e \psi_d \end{cases} \tag{1}$$

where i_d and i_q are *d*-axis and *q*-axis currents, respectively; u_d and u_q are *d*-axis and *q*-axis voltages; ψ_d and ψ_q are *d*-axis and *q*-axis flux linkages, respectively. ω_e is the electrical rotor angular frequency in rad/s. R_s is the stator armature resistance.

In practice, due to the nonlinear characteristic of the stator electric steel material, with different i_d and i_q the inductance L_d and L_q might change. Thus, the electrical dynamics of IPMSM can be rewritten as:

$$\begin{cases} u_d = R_s i_d + L_d\left(i_d, i_q\right)\dfrac{di_d}{dt} + i_d \dfrac{dL_d\left(i_d, i_q\right)}{dt} - \omega_e i_q L_q\left(i_d, i_q\right) \\ u_q = R_s i_q + L_q\left(i_d, i_q\right)\dfrac{di_q}{dt} + i_q \dfrac{dL_q\left(i_d, i_q\right)}{dt} \\ \qquad + \omega_e\left[i_d L_d\left(i_d, i_q\right) + \psi_f\right] \end{cases} \tag{2}$$

where $L_d(i_d,i_q)$ and $L_q(i_d,i_q)$ are the *d*-axis and *q*-axis inductances, respectively. ψ_f is the rotor's flux linkage.

For fulfilling FW control, a steady-state voltage and current limit curves are critical for the control design. The voltage limit curve can be derived based on Equation (2). When the IPMSM operates in MTPA and FW modes, a negative i_d will be injected in the *d*-axis, thus the saturation effect at *d*-axis can be neglected and L_d can be treated as a constant value [14]. Moreover, since the copper temperature coefficient is relatively small (0.39%/°C), the variation of R_s can also be neglected, and it can be considered as unchanged in the normal operation conditions. Therefore, the only parameter considered to change with i_d and i_q is the *q*-axis inductance L_q. Based on these considerations, the voltage limit in steady state can be derived from Equation (2) and is given as:

$$\left[R_s i_d - \omega_e i_q L_q\left(i_d, i_q\right)\right]^2 + \left[R_s i_q + \omega_e i_d L_d + \omega_e \psi_f\right]^2 \le {V_{max}}^2 \tag{3}$$

where V_{max} is the maximum voltage at the motor terminals that is determined by the DC-link voltage and the modulation strategy.

The current limit curve is dependent on the maximum current for the converter or the electrical machine and is given as:

$$i_d^2 + i_q^2 \le {I_{max}}^2 \tag{4}$$

In our case study, the current rating of voltage source inverter (VSI) is chosen higher than the maximum current of IPMSM considering the overcurrent in the transient process.

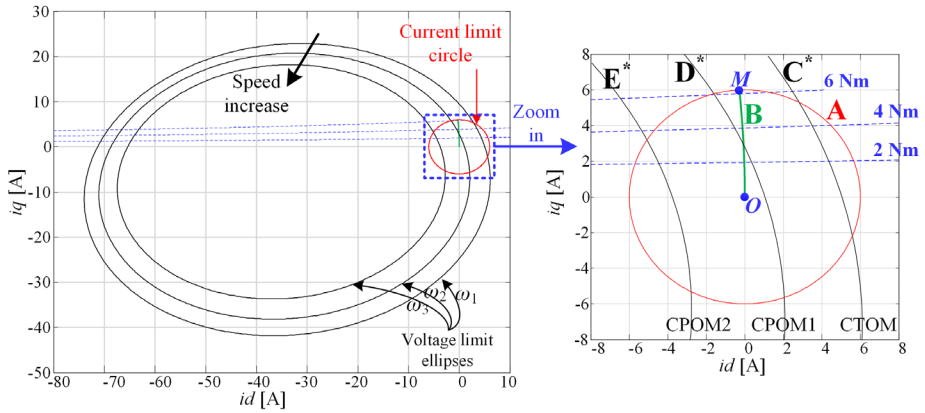

FIGURE 3 Current limit, voltage limit, and MTPA trajectory on *dq* plane: A—current limit circle; OBM—MTPA trajectory; C*—the voltage limit in constant torque operation mode; D*—the voltage limit in constant power operation mode 1, in which the voltage limit intersects with the MTPA, T_0 is the torque associated with the intersection point; E*–the voltage limit in constant power operation mode 2, in which the voltage limit does not intersect with the MTPA trajectory and the motor works in flux weakening mode even without load. $\omega_3 > \omega_2 > \omega_1$. Dashed lines: torque curves

The electromagnetic torque of the IPMSM is given as below, where p is the pole pairs of magnets on rotor:

$$T_e = 1.5p\left[\psi_f i_q + \left(L_d - L_q\right) i_d i_q\right] \tag{5}$$

To ensure efficient torque generation, the trajectory of MTPA is formulated as follows aiming to minimise the copper loss of IPMSM at a given value of torque:

$$\begin{cases} \min\left(i_d^2 + i_q^2\right) R_s \\ s.t. T_e = 1.5p\left[\psi_f i_q + \left(L_d - L_q\right) i_d i_q\right] \end{cases} \tag{6}$$

The analytical solution of Equation (6) can be derived as follows using the Lagrange multiplier method:

$$\begin{aligned} L\left(i_d, i_q, \lambda\right) = &\left(i_d^2 + i_q^2\right) R_s \\ &+ \lambda\left\{T_e - 1.5p\left[\psi_f i_q + \left(L_d - L_q\left(i_d, i_q\right)\right) i_d i_q\right]\right\} \end{aligned} \tag{7}$$

where λ is the Lagrange multiplier.

The partial derivative of Equation (7) can be expressed as follows:

$$\begin{cases} \dfrac{\partial L\left(i_d, i_q, \lambda\right)}{\partial i_d} = 2R_s i_d - 1.5p\lambda\left(L_d - L_q\right) i_q = 0 \\ \dfrac{\partial L\left(i_d, i_q, \lambda\right)}{\partial i_q} = 2R_s i_q - 1.5p\lambda\left[\psi_f + \left(L_d - L_q\right) i_d\right] = 0 \\ \dfrac{\partial L\left(i_d, i_q, \lambda\right)}{\partial \lambda} = T_e - 1.5p\left[\psi_f i_q + \left(L_d - L_q\right) i_d i_q\right] = 0 \end{cases} \tag{8}$$

Eliminating the parameter λ in Equation (8), the *dq*-axes current relation on MTPA curve can be derived as follows using a first-order Taylor series approximation for the ease of real-time implementation [20]:

$$i_d = \frac{L_d - L_q}{\psi_f} i_q^2 \tag{9}$$

TABLE 1 Main parameters of the IPMSM (Type: 115UMC300CACAA)

Parameter	Rated Value
Motor power	2.54 kW
Motor torque	8.1 N•m
Rated current	5.93A
Pole Pairs	1.3 Ω
Stator resistance at 25 °C	6.17 mH
d-axis stator inductance	0.23 Wb
Flux linkage of magnet	0.0077 kg·m^2
Moment of inertia	12.5 kHz
Switching frequency	

2.2 | Proposed control scheme for the MTPA and flux weakening operation

The constraints expressed in Equations (3) and (4) can be plotted in the *dq* plane in Figure 3 using the studied IPMSM parameters in Table 1. It can be seen that considering the impact of stator resistance, the voltages limit eclipses becomes asymmetric along with the real axis. It can also be noted that with the speed increasing, the eclipses will get smaller. Neglecting stator resistance as in [13] may lead to a simpler calculation. However, it is clear that such an assumption is not reasonable for high-performance IPMSM drives and the feedforward control techniques based on these assumptions may result in a compromised system performance.

In Figure 3, it can also be noted that the voltage limit eclipses shrink when the machine speed increases. Based on the

position of the voltage limit curve, three operation modes are defined, i.e. constant torque operation mode (CTOM), constant power operation mode 1 (CPOM1), and constant power operation mode 2 (CPOM2). The *d*-axis and *q*-axis current references for feedforward control will be dependent on different operation modes and will be discussed in the following sections.

2.2.1 | Case 1. Constant torque operation mode (CTOM)

As discussed before, when the speed increases, the speed limit eclipse will shrink. At a certain speed, the voltage limit will cross the MTPA point on the current limit curve (point *M* in Figure 3), this speed is defined as the base speed ω_b. Beyond this speed means the FW control will be necessary. The expression of ω_b is derived from Equations (3) and (9) as

$$\omega_b = \frac{-b + \sqrt{b^2 - 4ac}}{2a} \tag{10}$$

where, $a = [L_q(i_d, i_q)i_{qb}]^2 + (L_d i_{db})^2 + \psi_f{}^2 + 2L_d\psi_f i_{db}$, $b = 2[L_d - L_q(i_d, i_q)]R_s i_{db} i_{qb} + 2R_s\psi_f i_{qb}$, $c = R_s{}^2(i_{db}{}^2 + i_{qb}{}^2) - V_{\max}{}^2$, (i_{db}, i_{qb}) indicates the point *M* on the *dq* plane.

If the speed is less than ω_b, the voltage limit will enclose the MTPA trajectory (such as the curve *C** in Figure 3). In this case, the machine should operate on the MTPA trajectory at different loading conditions to achieve maximum efficiency.

In the proposed control scheme, the output of speed controller is the torque reference. In that case, the optimal *dq*-axes current references should be the intersection point of the MTPA trajectory and the torque curve. Combining the MTPA curve equation and torque equation will give us the analytical expression of optimal currents i_d and i_q. However, this explicit expression of the optimal i_d and i_q is difficult to derive and it is also challenging to implement such an expression into a digital control platform. To obtain the i_d and i_q values at the point where the MTPA trajectory crossing the torque curve online, a preceding-observation based method, i.e. Newton–Raphson algorithm, is adopted.

The optimal current i_d and i_q (i_d, i_q) under the CTOM operation condition can be derived by combining the torque curve (5) and MTPA trajectory (9):

$$F(x) = \begin{cases} \text{Torque}: f_1(i_d, i_q) \\ \quad = 1.5p\left[\psi_f i_q + \left(L_d - L_q(i_d, i_q)\right) i_d i_q\right] - T_e^{\text{ref}} = 0 \\ \text{MTPA}: f_2(i_d, i_q) = i_d - \dfrac{L_d - L_q(i_d, i_q)}{\psi_f} i_q{}^2 = 0 \end{cases} \tag{11}$$

Defining $\mathbf{x}^k = [i_d{}^k \; i_q{}^k]^T$, $\mathrm{F}(\mathbf{x}^k) = [f_1{}^k \; f_2{}^k]^T$, where *k* is the time sequence. Then Equation (11) can be solved using the Newton–Raphson algorithm with the iteration procedure given as follow

$$x^{k+1} = x^k - F'(x^k)^{-1} F(x^k), k = 1, 2, \ldots, n \tag{12}$$

where $F'(\mathbf{x}^k)$ is the Jacobi matrix of $F(\mathbf{x}^k)$, given as

$$F'(x^k) = \begin{bmatrix} \dfrac{\partial f_1}{\partial i_d} & \dfrac{\partial f_1}{\partial i_q} \\ \dfrac{\partial f_2}{\partial i_d} & \dfrac{\partial f_2}{\partial i_q} \end{bmatrix} = \begin{bmatrix} \dfrac{3p}{2}\left[\left(L_d - L_q\right) i_q - i_d i_q \dfrac{\partial L_q}{\partial i_d}\right] & \dfrac{3p}{2}\left[\psi_f + \left(L_d - L_q\right) i_d - i_d i_q \dfrac{\partial L_q}{\partial i_q}\right] \\ 1 + \dfrac{i_q{}^2}{\psi_f}\dfrac{\partial L_q}{\partial i_d} & -2\dfrac{L_d - L_q}{\psi_f} i_q + \dfrac{i_q{}^2}{\psi_f}\dfrac{\partial L_q}{\partial i_q} \end{bmatrix} \tag{13}$$

The partial derivatives of $L_q(i_d, i_q)$ can be obtained from the result of L_q identification that will be shown in Figure 10 in Section 3. The choice of the initial value $\mathbf{x}^0$ is crucial for the convergence of the Newton–Raphson method. A good start is to use $\mathbf{x}^0$ from the intersection of the torque curve and imagery axis, i.e. $x^0 = [0, \frac{T_e^{\text{ref}}}{1.5p\psi_f}]^T$. The proof of convergence can be found in Appendix.

2.2.2 | Case 2. Constant power operation mode 1 (CPOM1)

When the speed is beyond ω_b, the voltage limit curve can be represented as the curve *D** as an example in Figure 3. In this case, the maximum torque that machine produces at point *M* cannot be maintained due to the machine terminal voltage limitations. The operating point of the machine drive can be on either the MTPA trajectory or the voltage limit curve, depending on the torque command. The cross point of the MTPA and the voltage limit curves can be given as:

$$F(x) = \begin{cases} \text{VoltageLimit}: f_1(i_d, i_q) = \left[R_s i_d - \omega_e i_q L_q(i_d, i_q)\right]^2 \\ \quad + \left[R_s i_q + \omega_e i_d L_d + \omega_e \psi_f\right]^2 - V_{\max}{}^2 = 0 \\ \text{MTPA}: f_2(i_d, i_q) = i_d - \dfrac{L_d - L_q(i_d, i_q)}{\psi_f} i_q{}^2 = 0 \end{cases} \tag{14}$$

Again, let $\mathbf{x}^k = [i_d{}^k \; i_q{}^k]^T$, $\mathrm{F}(\mathbf{x}^k) = [f_1{}^k \; f_2{}^k]^T$. Denoting the cross point of MTPA trajectory and voltage limit D* as (i_{d0}, i_{q0}),

then (i_{d0}, i_{q0}) can be obtained by repeating the process as shown from Equation (12). Substituting (i_{d0}, i_{q0}) into the torque function (5), the corresponding torque T_0 can be obtained.

As can be seen from Figure 3, if T_e^{ref} is smaller than T_0, the IPMSM can still operate on the MTPA trajectory. However, if the torque command T_e^{ref} is larger than T_0, the MTPA cannot be reached, and the IPMSM operating states will stay on the voltage limit. In this case, the operational i_d and i_q can be calculated using the voltage limit curve and torque curve as follows:

$$F(x)=\begin{cases}\text{VoltageLimit}: f_1\left(i_d,i_q\right)=\left[R_s i_d-\omega_e i_q L_q\left(i_d,i_q\right)\right]^2 \\ \quad +\left[R_s i_q+\omega_e i_d L_d+\omega_e \psi_f\right]^2-{V_{max}}^2=0 \\ \text{Torque}: f_2\left(i_d,i_q\right) \\ \quad =1.5p\left[\psi_f i_q+\left(L_d-L_q\left(i_d,i_q\right)\right)i_d i_q\right]-T_e^{ref}=0\end{cases} \tag{15}$$

Thus, the optimal dq-axes reference (i_d^{ref}, i_q^{ref}) can be obtained using the Newton–Raphson algorithm as in Equation (12). If $T_e^{ref} < T_0$, the operation can still remain on the MTPA trajectory. In this scenario, the calculation process of dq-axes reference (i_d^{ref}, i_q^{ref}) is the same as that in Section B1, i.e. using Newton–Raphson algorithm to solve Equation (11).

2.2.3 | Case 3. Constant power operation mode 2 (CPOM2)

If the speed further increases from CPOM1, the voltage limit curve will keep shrinking. At one point, the voltage limit curve crosses the original point, i.e. (0,0). Beyond this speed, the voltage limit curve will be located on the left side of the origin (0,0) within the current limit curve. In this case, the operation curve will not intersect with the MTPA trajectory and the FW mode is always active. The threshold speed is denoted as ω_f and can be obtained by applying the origin (0, 0) into the voltage limit Equation (3). This gives a threshold speed ω_f as

$$\omega_f=\frac{V_{max}}{\psi_f} \tag{16}$$

One example of the voltage limit curve under CPOM2 is the curve E^* in Figure 3. It can be seen that E^* locates on the left side of the MTPA and with no intersection with the MTPA trajectory. The optimal operating point (i_d^{ref}, i_q^{ref}) under this scenario can be derived by combining the voltage limit and torque curve. The computation process is the same as that for the CPOM1 when $T_e^{ref} > T_0$ as shown in Equation (15).

2.3 | The output limitation of speed regulator

In conventional feedback FW methods, the d-axis current reference i_d^{ref} comes from the voltage controller, as shown in Figure 1. The reference current in the q-axis i_q^{ref} is limited by $\sqrt{{I_{max}}^2-{i_d}^{ref^2}}$ to avoid overcurrent. This constraint is essential to make sure that there is no overcurrent issues when the speed of IPMSM is beyond the base speed ω_b or a heavy load is applied.

Our proposed flux-weakening control method will also consider these current limitations. As discussed in the previous section, the dq-axes current references are calculated from T_e^{ref}, current/voltage limitation curves and MTPA curve using Newton–Raphson algorithm. This means that the dq-axes current references are not independently calculated and the limitation $i_q^{ref}=\sqrt{{I_{max}}^2-{i_d}^{ref^2}}$ is not suitable in our proposed method.

To deal with the issue, a new limitation method is developed for the proposed FW method. If the speed is below the base speed ω_b, this means the IPMSM is able to accelerate or decelerate with its maximum torque. The torque reference T_e^{ref} under this operation condition is equal to T_{e0}^{ref}, which is the output of speed controller. However, when the speed of IPMSM is over ω_b, the maximum torque cannot be generated and a torque limitation should be applied. In this case, the maximum torque is determined by the intersection point of the current limit curve and the voltage limit curve. i_d and i_q currents at this intersection point are noted as (i_{dmax}, i_{qmax}) and the associated maximum torque T_{emax} in this condition can be obtained from torque equation in (5).

With the derived T_{emax}, the control logic can be set as follows: if $T_{e0}^{ref} > T_{emax}$, the torque reference T_e^{ref} should be set to T_{emax}, or else the torque reference T_e^{ref} should be set to T_{e0}^{ref}.

The computation of (i_{dmax}, i_{qmax}) is similar as the process shown before. Let $\mathbf{x}^k=[i_d^k\ i_q^k]^T$, $\mathrm{F}(\mathbf{x}^k)=[f_1^k\ f_2^k]^T$, where:

$$F(x)=\begin{cases}\text{VoltageLimit}: f_1\left(i_d,i_q\right)=\left[R_s i_d-\omega_e i_q L_q\left(i_d,i_q\right)\right]^2 \\ \quad +\left[R_s i_q+\omega_e i_d L_d+\omega_e \psi_f\right]^2-{V_{max}}^2=0 \\ \text{CurrentLimit}: f_2\left(i_d,i_q\right)={i_d}^2+{i_q}^2-{I_{max}}^2=0\end{cases} \tag{17}$$

Repeating the procedure shown in Equation (12), i_d and i_q will converge to (i_{dmax}, i_{qmax}), which is the intersection point of the current limit and voltage limit curves.

3 | Q-AXIS INDUCTANCE IDENTIFICATION USING HF INJECTION METHOD

The i_d^{ref} and i_q^{ref} determination Equations (11), (14), (15), (17) all include the q-axis inductance L_q. Thus, the accuracy of L_q is crucial for the control performance and it is essential to obtain L_q at each operating point either online or offline. [26–29] have proposed different methods for L_q identification using recursive least squares algorithm, model reference adaptive method and extended Kalman filter. These methods depend on the d-axis steady state voltage equation to extract the apparent

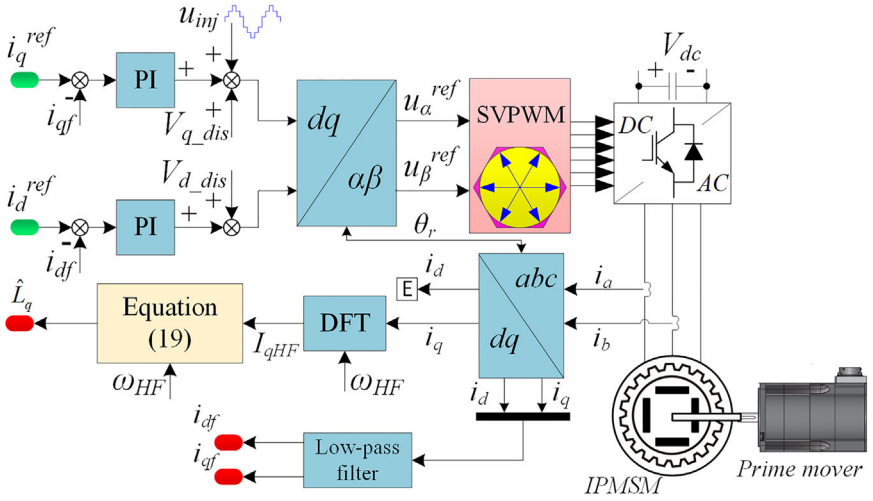

FIGURE 4 Diagram of proposed L_q identification method, where the low-frequency components i_{df} and i_{qf} are used for current control; high-frequency component I_{qHF} is used for L_q identification. V_{q_dis} and V_{d_dis} are from Figure 8 and 9

inductance in q-axis. Since the actual d-axis voltage cannot be physically measured, as instead the d-axis voltage reference is used to determine the apparent inductance. The d-axis voltage reference in digital control platform (in our case this is a DSP) is not a fixed value but fluctuated around an averaged value. Moreover, the measured stator current suffers from inevitable sampling noises and current transducer nonlinearity. Therefore, in the real-time calculation in DSP, both d-axis voltage reference and measured stator currents are fluctuated, resulting in fluctuation in the estimated apparent inductance. For the studied drive systems, the stator inductance is only several milli-Henry (mH), thus even one volt d-axis voltage error will lead to a noticeable static state identification error.

To address these issues, a high frequency (HF) injection method using a HF staircase voltage signal is proposed. The HF injection-based method exploits the high-frequency components to determine the incremental inductance, which presents a much higher accuracy than using the fundamental voltages and currents. The proposed method guarantees an excellent performance under low sampling ratio. The nonlinearity of VSI is also considered in the proposed method.

3.1 | Proposed strategy for q-axis inductance identification

The diagram of proposed L_q identification method is shown in Figure 4. As can be seen, a prime mover is used to drive the IPMSM with a controlled speed. i_d and i_q of the IPMSM can be actively controlled with current controllers. Different operation points with different i_d^{ref} and i_q^{ref} are given to create a full map of L_q. A high-frequency (HF) staircase voltage signal u_{inj} is superposed to the output of q-axis current controller. V_{d_dis} and V_{q_dis} are compensation voltages dealing with the VSI nonlinearities.

The current response due to injected HF voltage signals can be acquired from i_q using a signal processing scheme. The amplitude of HF component of q-axis current is calculated by the discrete Fourier transform (DFT), given as:

$$\begin{cases} \text{Re}_1 = \dfrac{2}{N}\left[i_q(0) + \displaystyle\sum_{n=1}^{N-1} i_q(n)\cos\left(\dfrac{2\pi n}{N}\right)\right] \\ \text{Im}_1 = \dfrac{2}{N}\left[-\displaystyle\sum_{n=0}^{N-1} i_q(n)\sin\left(\dfrac{2\pi n}{N}\right)\right] \\ I_{q\text{HF}} = \sqrt{\text{Re}_1{}^2 + \text{Im}_1{}^2} \end{cases} \tag{18}$$

where Re_1 and Im_1 are the real and imaginary components of the HF current, respectively. A low-pass filter (LPF) is used to derive the low frequency components in the i_d and i_q (i_{df} and i_{qf}) and feedback them to the current controller.

The estimated q-axis inductance $\hat{L}_q$ can be given as:

$$\hat{L}_q = \frac{U_{\text{inj}}}{I_{q\text{HF}}\omega_{\text{HF}}} \tag{19}$$

where U_{inj} and ω_{HF} are the amplitude and the angular frequency of the injected HF signal respectively.

3.2 | Analysis of the injected HF voltage signal

As explained in the previous section, a high-frequency signal with frequency ω_{HF} is used to estimate the inductance $\hat{L}_q$. Selecting a proper ω_{HF} is crucial to ensure the accuracy of the proposed method. If ω_{HF} is smaller than the bandwidth of current-loop, the injected signal will be suppressed by the current-loop and not be able to implement the q-axis inductance identification. Therefore, ω_{HF} should be set to be higher than the bandwidth of the current-loop.

Apart from the frequency, the sampling frequency ω_s of practical system should also be considered. As can be seen

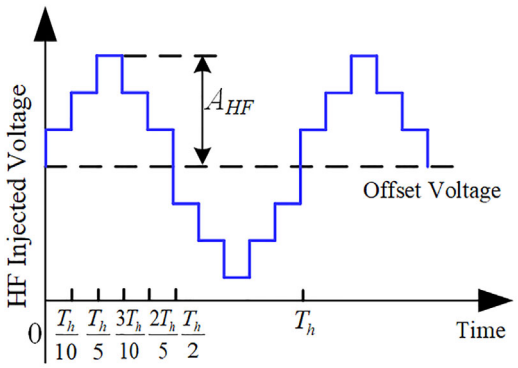

FIGURE 5 Waveform of the injected HF staircase voltage signal

in Table 1, the sampling frequency is 12.5 kHz. If ω_{HF} is too high, the ratio ω_s/ω_{HF} will decrease. This low sampling ratio will result in high and erratic harmonics in the injected signal and degrade the q-axis inductance identification performance. To deal with this issue, a staircase signal instead of conventional sinusoidal signal is designed as shown in Figure 5. For a 12.5 kHz sampling frequency control platform, the frequency of injected signal is chosen as 1,250 Hz with the ratio $\omega_s/\omega_{HF} = 10$. This means there are ten points in a cycle for the HF injected signal to the drive system.

For injected signal, the Fourier series can be given as:

$$u_{inj}(t) = \sum_{n=-\infty}^{+\infty} U_n e^{jn\omega_{HF}t} \tag{20}$$

where ω_{HF} is the frequency of injected signal, U_n is the coefficient of nth harmonics. As can be seen in Figure 5 the injected signal is odd symmetric, therefore n can be expressed as $n = 2k-1$, $k = 1, 2, 3$ etc. The coefficient U_n is given as:

$$U_n = \frac{2}{T_{HF}} \int_0^{T_{HF}} u_{inj}(t) e^{-jn\omega_{HF}t} dt = \frac{1}{\pi} \int_0^{2\pi} u_{inj}(\theta) e^{-jn\theta} d\theta \tag{21}$$

where T_{HF} is the period of injected HF signal, $\theta = \omega_{HF}t$.

From Equation (21), the absolute value of the coefficient of the injected signal can be obtained as

$$|U_n| = \left| \frac{j}{\pi n} \begin{pmatrix} e^{-jn\frac{7\pi}{5}} + e^{-jn\frac{6\pi}{5}} + e^{-jn\frac{4\pi}{5}} + e^{-jn\frac{3\pi}{5}} + 2e^{-jn\pi} \\ -e^{-jn\frac{9\pi}{5}} - e^{-jn\frac{8\pi}{5}} - e^{-jn\frac{2\pi}{5}} - e^{-jn\frac{\pi}{5}} - 2e^{-2jn\pi} \end{pmatrix} \right| \tag{22}$$

The amplitude of fundamental component can be calculated from Equation (22). As an example, for a HF injected staircase voltage with a maximum value $A_{HF} = 9$ V and an offset of 30 V as shown in Figure 5, the $|U_1| = 8.094$ V, i.e. the magnitude of fundamental component of u_{inj} is 8.094 V. This value is used in the following stator inductance identification procedure.

The designed staircase HF voltage signal and conventional sinusoidal voltage signal are both injected into the lab prototype IPMSM drive system on the q-axis, and the experimental responses of i_q are shown in Figure 6. Both injected signals are with 30 V DC offset to allow some initial values of i_q and the AC amplitude is 9 V. According to previous analysis, this means the magnitude of fundamental component of designed HF signal is 8.094 V. From Figure 6(a) it can be seen that the conventional sinusoidal signal presents a non-symmetric and distorted feature. The spectrum of the resulted i_q current is with more frequency harmonics (Figure 6(c)). Furthermore, the voltage magnitude of fundamental component of such a waveform is not easy to derive. This is mainly due to that the fundamental component is actually not constant and will be different each time running this identification algorithm. Hence, using conventional signal for L_q identification is not reliable.

As a contrast, the proposed staircase signal will result in a symmetric waveform as shown in Figure 6(b). The spectrum of this waveform is also much cleaner as shown in Figure 6(d). The estimated L_q can thus be calculated using the injected voltage and resulted q-axis current component at 1,250 Hz. With the example case, the magnitude of major component of i_q at 1,250 Hz is 0.134 A as shown in Figure 6(d). Hence, the estimated L_q can be calculated as follows:

$$\hat{L}_q = \frac{8.094 \text{ V}}{0.134 \times (2\pi \times 1250 \text{ Hz})} = 7.7 \text{ mH} \tag{23}$$

In Figure 6(c, d), another component at 300 Hz can be observed. This is caused by the coupled DC machine as a three-phase diode rectifier is used to feed the DC machine.

3.3 | Analysis of VSI nonlinearity effect on inductance identification and compensation

It is well-known that power converters have nonlinearity characteristics, such as dead time, parasitic capacitances, control signal delay, and on-state voltage drop power module. These nonlinear behaviours usually lead to distortions of the injected HF voltage signal, and therefore undermine the identification accuracy. Among all the nonlinear effects, the dead time and parasitic capacitance effects are known to be the major contributors to voltage distortions [21, 22]. Therefore, appropriate compensation scheme should be considered and applied to improve the inductance identification accuracy.

Running the electrical drive with only the current loop and applying inverse Clark and Park transformations gives:

$$\begin{bmatrix} i_a^{ref} \\ i_b^{ref} \\ i_c^{ref} \end{bmatrix} = \begin{bmatrix} 1 & 0 \\ -1/2 & \sqrt{3}/2 \\ -1/2 & \sqrt{3}/2 \end{bmatrix} \begin{bmatrix} \cos\theta_r & \sin\theta_r \\ -\sin\theta_r & \cos\theta_r \end{bmatrix} \begin{bmatrix} i_d^{ref} \\ i_q^{ref} \end{bmatrix} \tag{24}$$

Considering the rotor is locked at angle $\theta_r = 0$ and a positive i_d current ($i_d^{ref} > 0$, $i_q^{ref} = 0$) is applied to the IPMSM, Equation (24) will give the result $i_a^{ref} = i_d^{ref}$, $i_b^{ref} = i_c^{ref} = -i_d^{ref}/2$. In this case, one of the N-poles of the rotor is aligned with the

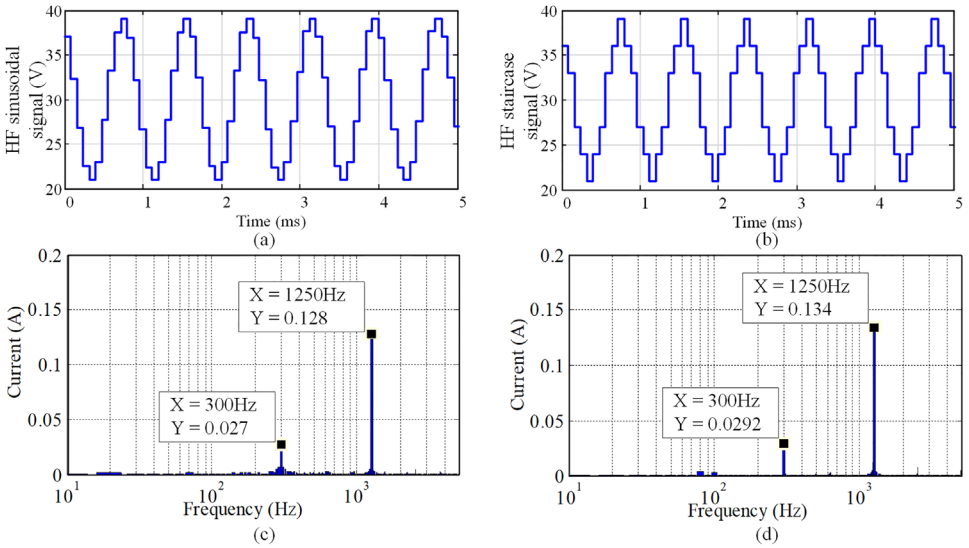

FIGURE 6 Experimental results of different injected voltage signals on *q*-axis and i_q responses. (a) conventional sinusoidal signal, 1,250 Hz; (b) the proposed staircase signal, 1,250 Hz; (c) the frequency characteristic of *iq* with sinusoidal signal; (d) the frequency characteristic of *iq* with proposed staircase signal

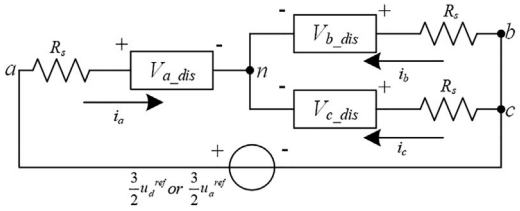

FIGURE 7 Equivalent circuit of IPMSM drive system when $\theta_r = 0$, $i_d^{ref} > 0$, $i_q^{ref} = 0$

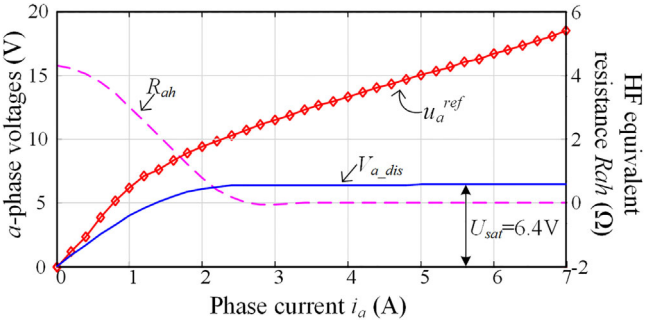

FIGURE 8 Experimental results of voltage reference u_a^{ref}, voltage error V_{a_dis}, and the HF equivalent resistance R_{ah}

a-phase of the stator. Since the IPMSM is standstill, the back-electromotive force (EMF) is zero. In addition, the three phase currents are all DC variables. Therefore, the voltage drop on each phase inductance is also zero. Under these conditions, the IPMSM can be seemed as a three-phase resistive load, thus we have:

$$\begin{cases} u_d^{ref} > 0, u_q^{ref} = 0 \\ u_a^{ref} = u_d^{ref}, u_b^{ref} = u_c^{ref} = -\frac{1}{2}u_d^{ref} \end{cases} \tag{25}$$

With Equation (25), considering the fact that the currents can actually track their references due the close-loop control, an equivalent circuit of an IPMSM drive system under $\theta_r = 0$, $i_d^{ref} > 0$, $i_q^{ref} = 0$ conditions can be drawn in Figure 7, where V_{a_dis}, V_{b_dis} and V_{c_dis} are the distorted voltages caused by the VSI nonlinearities on phase *a*, phase *b* and phase *c* respectively.

Applying the Kirchoff's voltage law to the circuit in Figure 7, the following equation can be derived:

$$R_s i_a + V_{a\_dis} - V_{b\_dis} - R_s i_b = \frac{3}{2}u_d^{ref} \tag{26}$$

Substituting $i_b^{ref} = -i_a^{ref}/2$, $u_a^{ref} = u_d^{ref}$ in Equations (25) to (26) and assuming that the power module of each phase leg is of the same physical characteristic (i.e. $V_{a\_dis} = -V_{b\_dis}$), we have

$$V_{a\_dis} = \frac{3}{4}\left(u_a^{ref} - R_s i_a\right) \tag{27}$$

With Equation (27) and considering the fact that $i_a = i_d$, and thus $i_a^{ref} = i_d^{ref}$ (since the drive is with closed-loop current control), we can increase the i_d^{ref} gradually and record the corresponding u_d^{ref}. The u_d^{ref} is essentially equal to u_a^{ref}. Then the relation between i_a^{ref} and u_a^{ref} can be derived. From Equation (27), it can be derived that R_s is actually the slope of u_a^{ref}. Thus R_s can be calculated as:

$$R_s = \frac{du_a^{ref}}{di_a^{ref}} \approx \frac{\Delta u_a^{ref}}{\Delta i_a^{ref}} = \frac{\Delta u_d^{ref}}{\Delta i_d^{ref}} \tag{28}$$

Figure 8 shows the experimental results using the IPMSM lab prototype shown in Figure 12 with i_d^{ref} (i.e. i_a^{ref}) increased from

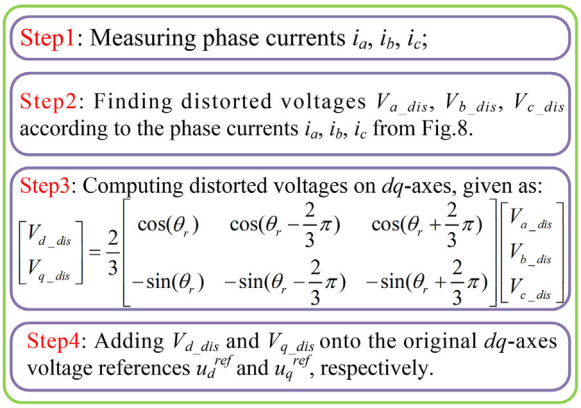

FIGURE 9 The flowchart of VSI nonlinearity compensation procedure

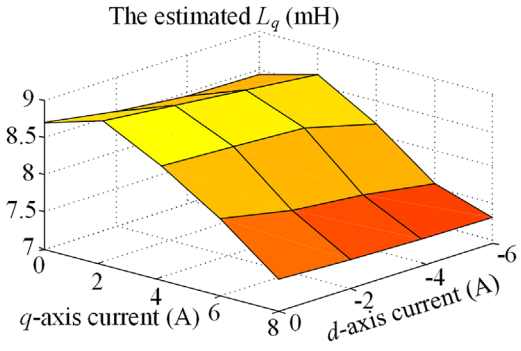

FIGURE 10 Experimental results of the estimated L_q with the proposed HF voltage signal injection and the VSI nonlinearity compensation

0 to 7 A with a step of 0.2 A. The rotor is locked and only inner current loop is executed to make dq current responses track their setpoints. The red dotted line is the sampled u_d^{ref} (i.e. u_a^{ref}) from real-time calculation in DSP. Using Equations (27) and (28), the distorted voltage V_{a_dis} can be obtained. It can be seen that in the low current region, V_{a_dis} will approximately linearly increase with i_a^{ref}. In the large current area, V_{a_dis} is saturated at 6.4 V for the studied IPMSM drive system.

Apart from R_s, within the HF injection scheme, the effect of parasitic capacitances should also be considered [21, 23]. Its effect can be modelled as a nonlinear HF equivalent resistance R_{ah}. As can be seen in (27), since the voltage error V_{a_dis} can be expressed as the function of i_a, their relation can be written as $V_{a\_\text{dis}} = f(i_a)$. With HF current injection, the a-phase current i_a contains the fundamental component i_{af} and the high frequency component i_{ah} associated with the HF injected voltage signal. Hence $i_a = i_{af} + i_{\text{ah}}$. Thus V_{a_dis} can be expressed using the following equation using Taylor-expansion at operation point i_{af}

$$V_{a\_\text{dis}} = f(i_a) = f(i_{af} + i_{\text{ah}}) \approx f(i_{af}) + f'(i_{af})i_{\text{ah}} \approx sign(i_{af})U_{\text{sat}} + R_{\text{ah}}i_{\text{ah}} \quad (29)$$

where i_{af} is the fundamental component of i_a, i_{ah} is the high frequency component of i_a associated with the injected signal. From Equation (29) and recalling V_{a_dis} in Figure 8, it can be concluded that U_{sat} is actually the saturation value of V_{a_dis} in Figure 8. R_{ah} is the HF resistance which is nonlinear to i_{af} and shown with the dashed line in Figure 8. Considering the U_{sat} is the same for all three phases, the compensation voltages V_{a_dis}, V_{a_dis}, and V_{a_dis} can be obtained by using phase currents as searching index. This compensation procedure of VSI nonlinearity is shown in Figure 9.

Based on the HF voltage injection method and the VSI nonlinearity compensation, the q-axis inductance of the IPMSM used in this paper can be obtained at various operation points. The experimental result of L_q identification is shown in Figure 10, where i_d changes from 0 to −6 A and i_q varies from 0 to 8 A. Each operating point is achieved by executing the current loop control. As can be seen in Figure 10, when i_q changes from 0 to 2 A, L_q increases due to the alignment of the magnetic domains in the stator core. However, when i_q keeps increasing, L_q will decrease due to the magnetic saturation. i_d will also affect L_q through cross coupling effect. The off-line identified data in Figure 10 is implemented into the DSP as a look-up table for the proposed FW method.

The developed control scheme can be summarised and shown in Figure 11. With the developed feedforward FW control technique and identified L_q map, an improved performance can be achieved and will be demonstrated in the next section.

4 | EXPERIMENTAL RESULTS

4.1 | Experimental setup

To validate the developed feedforward FW control scheme, an experimental setup is established. The test rig consists of a DC motor drive as a load, an IPMSM machine, a two-level power converter and its control. The parameters of the IPMSM machine are shown in Table 1.

The hardware structure of test rig is shown in Figure 12(a) and the operating procedure of the system with proposed feedforward FW scheme is shown in Figure 12(b). A 300 V DC bus voltage is provided by a bi-directional DC power source. The DSP/FPGA platform is used for control algorithm implementation and signal measurements. The communication between the PC and the DSP is realised by a DSKc6713 board. The sampling and control period are 80 μs (i.e. 12.5 kHz). During experiments, important variables, such as speed and currents are uploaded to the PC via HPI daughter board and are plotted in the Matlab.

Both speed-loop and current-loop adopt PI controllers. The design process of PI gains of current controller can refer to [32] with 1 kHz bandwidth and 0.707 damping ratio. The current limitation I_{max} is set as 6 A. $\omega_{\text{b}} = 212.16$ rad/s, $\omega_{\text{f}} = 226.09$ rad/s. In addition, control margins are set for each algorithm. For the feedback FW method, the maximum

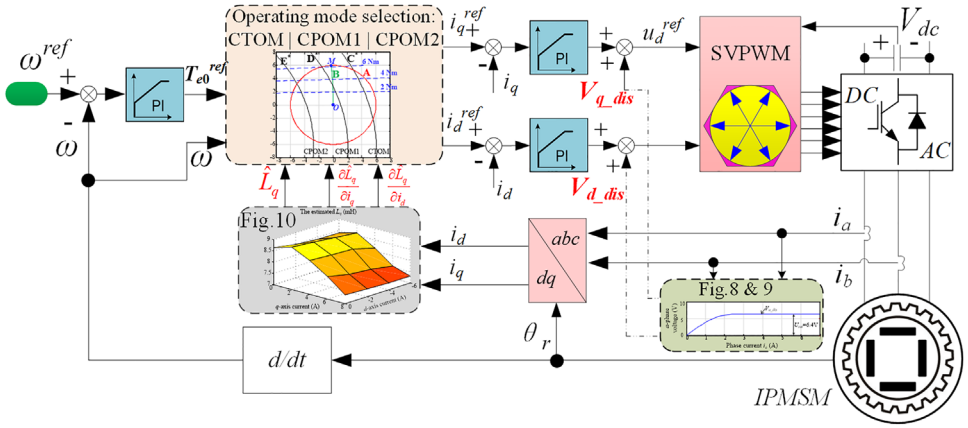

FIGURE 11 Control block diagram with the proposed flux weakening control scheme considering inductance variation

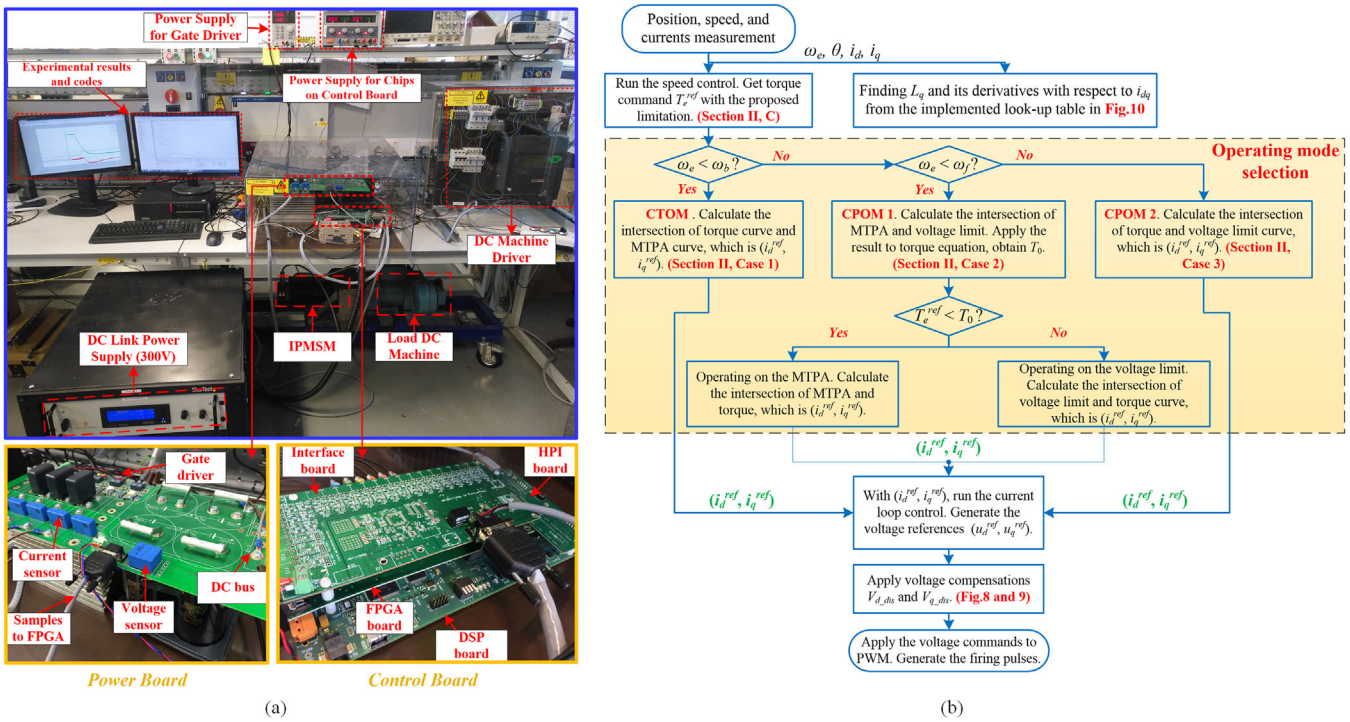

FIGURE 12 Test rig and control algorithm flowchart. (a) The experimental rig setup. (b) Operating procedure of the IPMSM control with the proposed FW method

utilised voltage is 0.57 $V_{dc}(V_{dc}/\sqrt{3})$ which is the inscribed circle of voltage hexagon. Here V_{max} is set as 0.52 V_{dc}, with a 10% margin [30]. While for the feedforward FW methods, the control margin can be tuned by scaling the speed feedback [31]. In this paper the speed fed to the feedforward FW methods is set as 105% × ω_m, where ω_m is the mechanical angular speed provided by the encoder. In the following, the feedback FW method shown in Figure 1 and the feedforward method which ignores the stator resistance and magnetic saturation are referred as PI method and conventional feedforward (CFF) method. Performances of these three control schemes are compared.

4.2 | Performance comparison of proposed method, PI method and CFF method

The performances in a speed step change are shown in Figure 13. From top to bottom: mechanical speed command and response; *dq*-axes currents; the flag indicates operation condition and the modulation indexes (MI); and the execution time of algorithm. The final MI is the one that used in space vector PWM (SVPWM), and the equivalent MI is defined as $\sqrt{3}\cdot\sqrt{{u_d}^{\text{ref}^2}+{u_q}^{\text{ref}^2}}/V_{dc}$. The current responses shown in Figure 13(a2,b2,c2) are redrawn in the *dq* plane in Figure 14.

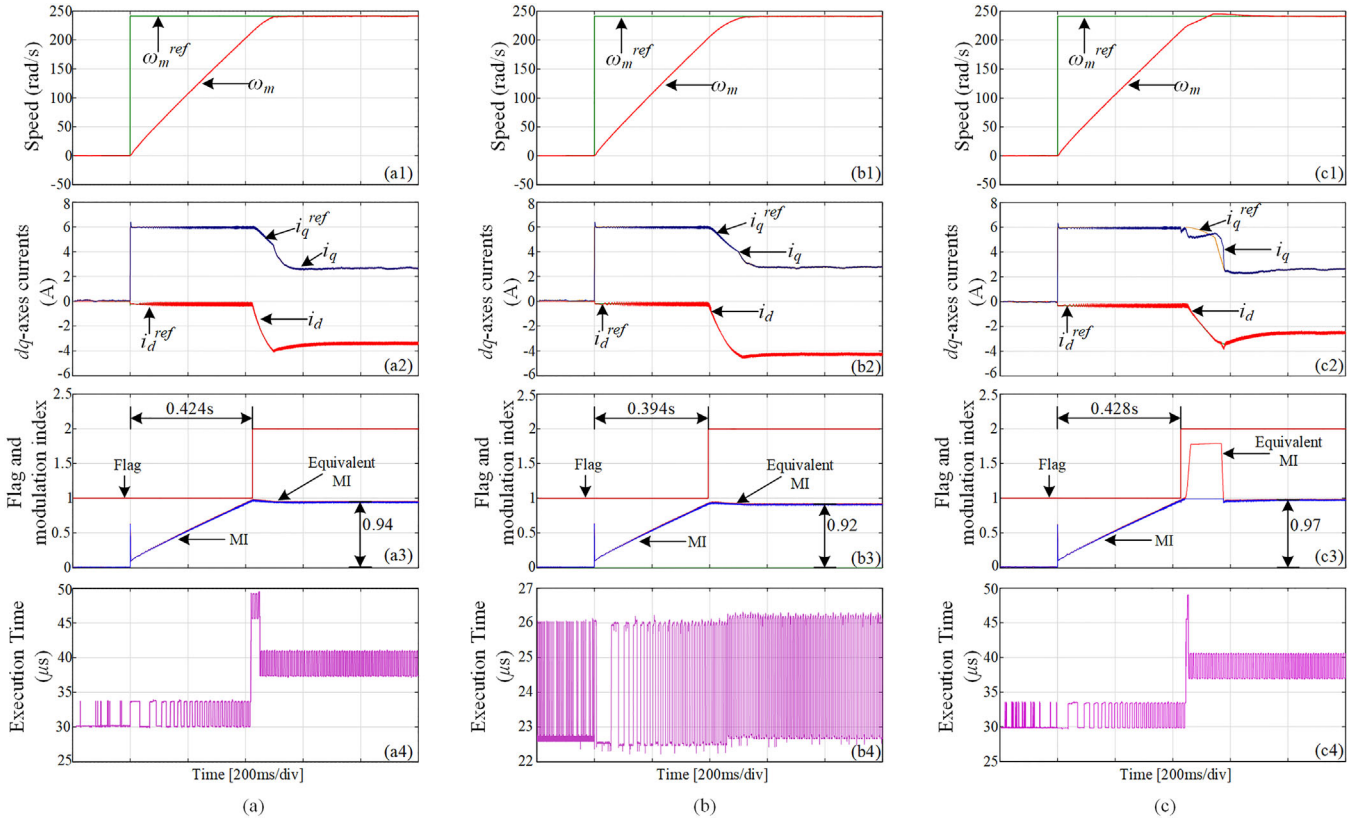

FIGURE 13 Experimental responses to speed step change from 0 to 2300 r/min (240.86 rad/s) with 2.4 Nm load. (a) proposed method; (b) PI method; (c) CFF method. From top to bottom: mechanical speed command and response; *dq*-axes currents; the flag indicates operation condition and the modulation index; and the execution time of each algorithm. ω_b = 212.16 rad/s, ω_f = 226.09 rad/s

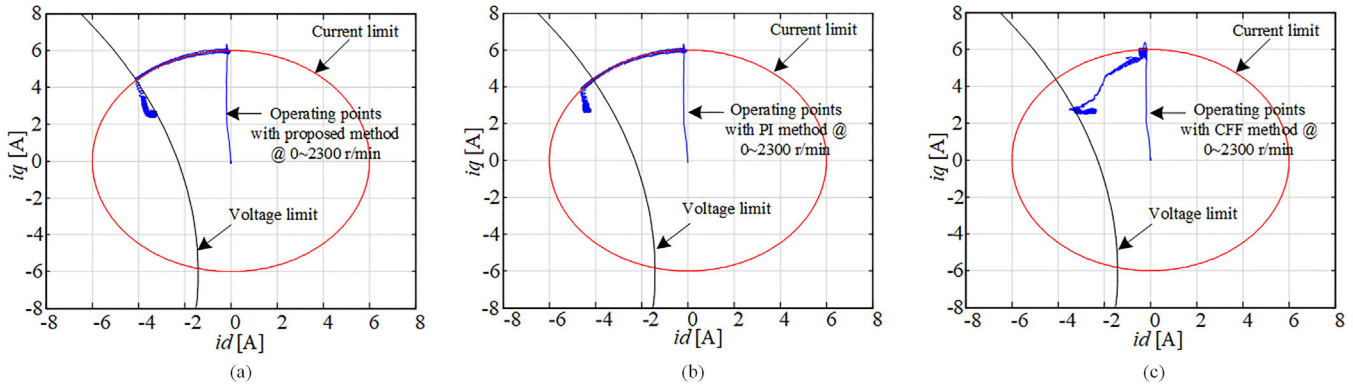

FIGURE 14 Trajectories of *dq*-axes current response. (a) proposed method; (b) PI method; (c) CFF method

4.2.1 | Comparison of proposed method and PI method

Firstly, the proposed FW method and the PI method are compared. Their performances are shown in Figure 13(a, b), respectively. It can be seen that below base speed, maximum torque is generated and the IPMSM operates in the CTOM mode. When the speed is over the base speed, a negative *d*-axis current is injected into the machine to guarantee the power output. In this case the IPMSM operates in the CPOM1. Transient responses of these two methods are similar. However, in the steady state, the magnitude of i_d of PI method is −4.2 A, larger than −3.5 A of proposed method. If the control margin for PI method is set smaller than 10%, the magnitude of i_d will decrease since DC bus voltage utilisation is improved. However, this is at the expense of a low motion dynamics. Besides, the control

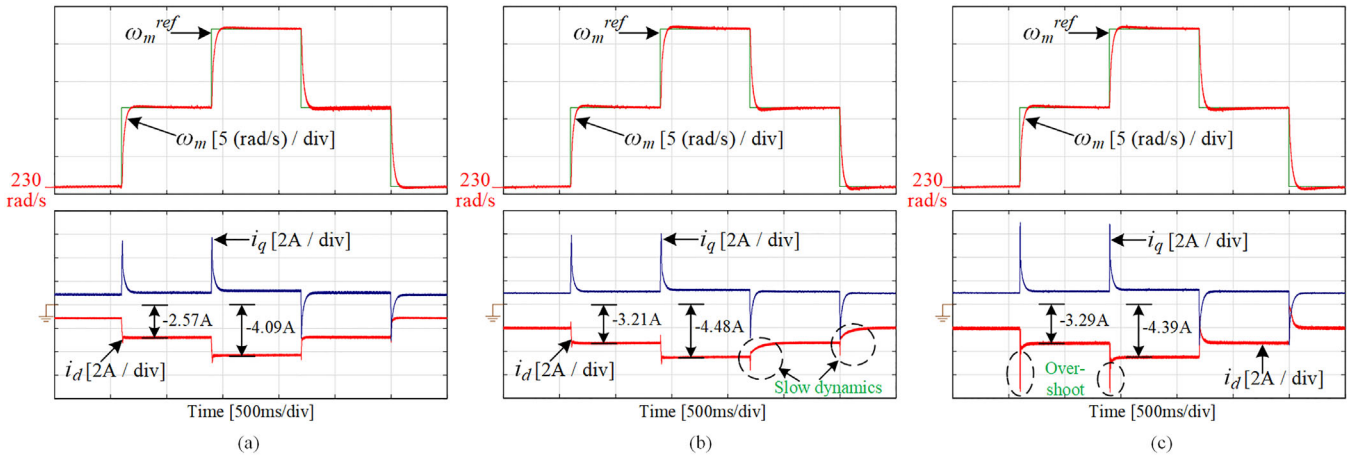

FIGURE 15 Experimental responses when speed step changes from 2,200 r/min (230.38 rad/s) to 2,300 r/min (240.85 rad/s) to 2,400 r/min (251.33 rad/s) to 2,300 to 2,200 r/min. (a) proposed FW method; (b) PI method with $k_{pv} = 0.5$, $k_{iv} = 20$; (c) PI method with $k_{pv} = 2$, $k_{iv} = 80$

margin cannot be set too small due to the voltage loss caused by dead-time effect and the voltage drop on power devices [31]. Therefore, when the control margin is set as the normal value 10%, the proposed FW method is better than PI method since a larger DC bus voltage can be utilised and therefore a smaller FW current i_d is needed. The reduction of current is beneficial for decreasing power losses in IPMSM. For the same reason, as can be seen in Figure 13(a3, b3) that the proposed FW method switches to FW control mode later than PI method.

The computation time for each method is also evaluated. It includes sampling, speed and current loop control, FW control, SVPWM and protections. As can be seen from Figure 13(a4,b4) that the execution time of proposed method is longer than PI method. However, the proposed FW method can still be comfortably calculated using our DSP/FPGA control platform.

Differences can also be observed in *dq* plane. In Figure 14(a), the machine initially accelerates with maximum torque. As the speed goes over the base speed, the operating points move along the current limit circle. When speed reaches 2,300 r/min, the operating points settle close to the boundary of voltage limit in the steady state. However, for the PI methods in Figure 14(b), the operating points stay far away from the voltage limit in the steady state thus a smaller DC voltage utilisation rate is achieved.

To compare the dynamic performances, a speed variation test is conducted as shown in Figure 15, where k_{pv} and k_{iv} are the PI gains of outer voltage loop of the PI method. If k_{pv} and k_{iv} are set to be small in Figure 15(b), the i_d transient response will be slower than that of proposed method in Figure 15(a). While if k_{pv} and k_{iv} are set to be large, large current overshoot will occur as shown in Figure 15(c). As the selection of k_{pv} and k_{iv} are normally using trial and error method, it can be very difficult to achieve the optimal design. As a contrast, in the proposed FW method there is no need to tune such PI parameters. As long as the IPMSM's machine parameters are fed, optimal *dq*-axes current setpoints can be generated in a fast fashion without overshoot as shown in Figure 15(a).

4.2.2 | Performance comparison of proposed method and CFF method

The comparison of the proposed method and the CFF method is discussed in this session. For the CFF method, when it works from CTOM to CPOM1, the actual i_q will deviate from i_q^{ref} as shown in Figure 13(c2). Since the effect of stator armature resistance and magnetic saturation are neglected in the CFF method, during the transient state the system cannot follow the current commands. The oscillation in i_q will lead to the oscillation in toque, making the speed unsmooth in transient process as shown in Figure 13(c1). Moreover, due to the deviation between the current reference and the feedback, the current controller will saturate. Additionally, as can be observed in Figure 14(c), during the transients the operating points are not located on the boundary of current limit circle. Therefore, compared with proposed method as shown in Figure 14(a), the maximum available torque is not fully utilised.

4.3 | Steady state operation of proposed FW method

In this subsection the steady state performance of proposed FW method is evaluated. A few different operation points (speed and load torque, marked with A-H in Figure 16) are selected in the experiment. The results show that when the machine speed n is smaller than ω_b, the proposed FW method can guarantee the IPMSM operates on the MTPA trajectory in CTOM mode (operation conditions A, B, C). When $\omega_b < n < \omega_f$, the IPMSM will work on MTPA when outputs small torque but operate on the boundary of voltage limit at large torque in CPOM1 (D, E, F). While if $n > \omega_f$, the IPMSM will always operate close to the boundary of voltage limit in the FW mode in CPOM2 (G, H). The results confirm the effectiveness of proposed FW method at different speeds and load conditions.

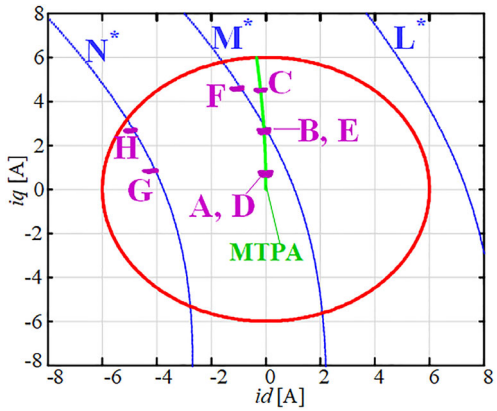

FIGURE 16 Experimental results of steady state operation points of proposed FW method, where ω_b is 212.16 rad/s (2,025.98 r/min), $\omega_f = 226.09$ rad/s (2,159.00 r/min). (A) 1,800 r/min, 0 Nm; (B) 1,800 r/min, 2 Nm; (C) 1,800 r/min, 4 Nm; (D) 2,100 r/min, 0 Nm; (E) 2,100 r/min, 2 Nm; (F) 2,100 r/min, 4 Nm; (G) 2,400 r/min, 0 Nm; (H) 2,400 r/min, 2 Nm; (L^*) voltage limit at 1,800 r/min; (M^*) voltage limit at 2,100 r/min; (N^*) voltage limit at 2,400 r/min. Red circle: current limit circle

5 | CONCLUSION

In this paper an improved feedforward FW method for IPMSM is proposed aiming for high-speed drive application considering the stator resistance and magnetic saturation effect. The optimal i_d and i_q current references in both constant torque region and constant power region are calculated online using Newton–Raphson algorithm. A new limitation approach of speed regulator output is proposed for generating proper torque command when the IPMSM operates in high speed and heavy load condition. In addition, a staircase signal is introduced and used in the high frequency injection method for L_q identification. The nonlinear effects of VSI are compensated for improving the accuracy of L_q identification.

Experimental results show that compared with the PI method, the proposed method can effectively improve DC voltage utilisations and the dynamic performance. This will be beneficial for reducing power losses in transmission cable and IPMSM. Such a feature is favourable in industrial application where efficiency is a major concern. Moreover, compared with CFF method, the proposed FW method can guarantee desirable transient performance and fully utilise the maximum available torque.

ACKNOWLEDGMENT

This project has received funding from the Clean Sky 2 Joint Undertaking under the European Union's Horizon 2020 research and innovation program under grant agreement No 807081. The author Xiaoyu Lang also thanks the stipend funding from China Scholarship Council (CSC).

NOMENCLATURE

$\hat{L}_q$	The estimated q-axis inductance
i_d, i_q	Stator currents (d,q axis, respectively)
I_{max}	The limitation value of stator current
k	Sample time instant
L_d, L_q	Stator inductance (d,q axis, respectively)
R_s	Stator resistance
T_e	Electromagnetic torque
u_d, u_q	Stator voltages (d,q axis, respectively)
V_{d_dis}, V_{q_dis}	The voltage distortion caused by power converter nonlinearity
V_{dc}	DC bus voltage
V_{max}	The limitation value of stator voltage
ψ_f	Rotor flux linkage
ω_e	Electrical rotor speed

REFERENCES

1. Liang, J., et al.: Optimization of air-gap profile in interior permanent-magnet synchronous motors for torque ripple mitigation. IEEE Trans. Transport. Electrific. 5(1), 118–125 (2019)
2. Du, B., et al.: Interturn fault diagnosis strategy for interior permanent-magnet synchronous motor of electric vehicles based on digital signal processor. IEEE Trans. Ind. Electron. 63(3), 1694–1706 (2016)
3. Islam, M.S., et al.: Asymmetric bar winding for high-speed traction electric machines. IEEE Trans. Transport. Electrific. 6(1), 3–15 (2020)
4. Alaei, A., et al:. Reduction of high-frequency injection losses, acoustic noise and total harmonic distortion in IPMSM sensorless drives. IET Power Electron. 12(12), 3197–3207 (2019)
5. Arumugam, P., et al.: High-speed solid rotor permanent magnet machines: Concept and design. IEEE Trans. Transport. Electrific. 2(3), 391–400 (2016)
6. Madonna, V., Giangrande, P., Galea, M.: Electrical power generation in aircraft: Review, challenges and opportunities. IEEE Trans. Transport. Electrific. 4(3), 646–649 (2018)
7. Li, C., et al.: A modified neutral point balancing space vector modulation for three-level neutral point clamped converters in high-speed drives. IEEE Trans. Ind. Electron. 66(2), 910–921 (2019)
8. Bozhko, S., et al.: Flux-weakening control of electric starter–generator based on permanent-magnet machine. IEEE Trans. Transport. Electrific. 3(4), 864–877 (2017)
9. Su, J., Gao, R., Husain, I.: Model predictive control based field-weakening strategy for traction EV used induction motor. IEEE Trans. Ind. Appl. 54(3), 2295–2305 (2018)
10. Wang, B., et al.: Speed-sensorless induction machine control in the field-weakening region using discrete speed-adaptive full-order observer. IEEE Trans. Power Electron. 31(8), 5759–5773 (2016)
11. Zhang, X., et al.: Analysis and optimization of current dynamic control in induction motor field-weakening region. IEEE Trans. Power Electron 35(9), 8860–8866 (2020)
12. Tursini, M., Chiricozzi, E., Petrella, R.: Feedforward flux-weakening control of surface-mounted permanent-magnet synchronous motors accounting for resistive voltage drop. IEEE Trans. Ind. Electron. 57(1), 440–448 (2010)
13. Preindl, M., Bolognani, S.: Model predictive direct torque control with finite control set for PMSM drive systems-part 2: Field weakening operation. IEEE Trans. Ind. Informat. 9(2), 648–657 (2013)
14. Jo, C., Seol, J.Y., Ha, I.J.: Flux-weakening control of ipm motors with significant effect of magnetic saturation and stator resistance. IEEE Trans. Ind. Electron. 55(3), 1330–1340 (2008)
15. Ge, H., et al.: Speed range extended maximum torque per ampere control for pm drives considering inverter and motor nonlinearities. IEEE Trans. on Power Electron. 32(9), 7151–7159 (2017)
16. Hu, D., Xu, L.: Characterizing the torque lookup table of an IPMSM machine for automotive application. In: *2014 IEEE Conference and Expo Transportation Electrification AsiaPacific (ITEC AsiaPacific)*, pp 1–6. IEEE, Piscataway, NJ (2014)

17. Chen, Y., et al.: Improved flux-weakening control of IPMSMSMs based on torque feedforward technique. IEEE Trans. Power Electron. 33(12), 10970–10978, (2018)
18. Cheng, B., Tesch, T.R.: Torque feedforward control technique for permanent-magnet synchronous motors. IEEE Trans. On Ind. Electron. 57(3), 969–974 (2010)
19. Bae, B.-H., et al.: New field weakening technique for high saliency interior permanent magnet motor. In: *38th IAS Annual Meeting on Conference Record of the Industry Applications Conference*, pp. 898–905. IEEE, Piscataway, NJ (2003)
20. Li, K., Wang, Y.: Maximum torque per ampere (MTPA) control for IPMSM drives using dignal injection and an MTPA control law. IEEE Trans. Ind. Informatics 15(10), 5588–5598 (2019)
21. Gong, L.M., Zhu, Z.Q.: A novel method for compensating inverter nonlinearity effects in carrier signal injection-based sensorless control from positive-sequence carrier current distortion. IEEE Trans. Ind. Appl. 47(3), 1283–1292 (2011)
22. Park, Y., Sul, S.-K.: A novel method utilizing trapezoidal voltage to compensate for inverter nonlinearity. IEEE Trans. Power Eletron. 27(12), 4837–4846 (2012)
23. Wang, G., et al.: Self-commissioning of permanent magnet synchronous machine drives at standstill considering inverter nonlinearities. IEEE Trans. Power Electron. 29(12), 6615–6627 (2014)
24. Deuflhard, P.: Newton Methods for Nonlinear Problems—Affine Invariance and Adaptive Algorithms. Springer, Berlin, Heidelberg (2004)
25. Ciarlet, P.G., Mardare, C.: On the Newton–Kantorovich theorem. Analysis and Applications 10(3), 249–269 (2012)
26. Long, J., et al.: Current-controller-free self-commissioning scheme for deadbeat predictive control in parametric uncertain SPMSM. IEEE Access 9, 289–302 (2021)
27. Zhu, Z.Q., Zhu, X., Sun, P.D.: Estimation of winding resistance and PM flux-linkage in brushless AC machines by reduced-order extended Kalman filter. In: *Proc. IEEE Int. Conf. on Networking, Sensing and Control*, pp. 740–745. IEEE, Piscataway, NJ (2007)
28. Liu, K., et al.: Influence of nonideal voltage measurement on parameter estimation in permanent-magnet synchronous machines. IEEE Trans. Ind. Electron. 59(6), 2438–2447 (2012)
29. Wang, Q., et al.: Offline parameter self-learning method for general-purpose PMSM drives with estimation error compensation. IEEE Trans. Power Electron. 34(11), 11103–11115 (2019)
30. Kwon, Y.-C., Kim, S., Sul, S.-K.: Six-step operation of PMSM with instantaneous current control. IEEE Trans. Ind. Appl. 50(4), 2614–2625 (2014)
31. Nalepa, R., Orlowska-Kowalska, T.: Optimum trajectory control of the current vector of a nonsalient-pole PMSM in the field-weakening region. IEEE Trans. Ind. Electron. 59(7), 2867–2876 (2012)
32. Burgos, R., et al.: Mathematical model and control design for sensorless vector control of permanent magnet synchronous machines. In: *Proc. of IEEE Workshops COMPEL*, pp. 76–82. IEEE, Piscataway, NJ (2006)

How to cite this article: Lang X., et al.: An enhanced feedforward flux weakening control for high-speed permanent magnet machine drive applications. IET Power Electron. 1–15. (2021) https://doi.org/10.1049/pel2.12170.

APPENDIX

Here, we only prove the case that the IPMSM operates in the CPOM2. The proof of CTOM and CPOM1 is similar to this one and won't be illustrated due to limited spaces.

The proof of convergence adopts the Newton–Kantorovich theorem [24, 25]. The theorem can be stated as follows: Given a n-dimension Banach space $\mathbb{R}^n$, an open subset $X \subset \mathbb{R}^n$, let the initial value satisfy $x^0 \in X$, and a nonlinear functions $F(x^k)$ with a Jacobian $F'(x^k)$ is continuous on X. Assuming that for open set $U \subset X$ there always exists a positive constant r such that:

$$\left\| F'(w) - F'(v) \right\| \le r \left\| w - v \right\| \; w, v \in U \qquad \text{(A1.)}$$

Then the sequence $\mathbf{x}^k$ which is defined by Equation (12) is such that $\mathbf{x}^k \in B(x^0;\, 1/r)$ for all $k \ge 0$ and converges to a zero $x^* \in B(x^0;\, 1/r)$, where B represents a close ball, if and only if following equation is satisfied:

$$r \left\| F'\left(x^0\right)^{-1} F\left(x^0\right) \right\| \le \frac{1}{2} \qquad \text{(A.2)}$$

In CPOM2, the mechanical speed should be larger than ω_f which is 226.09 rad/s, namely 2159.00 r/min. For speed from 2250 to 2500 r/min, torque command from −5 to 5 Nm, the minimum r which satisfies Equation (A.1) for all states w, $v \in$ CPOM2 is plotted as Figure A.1(a).

In Figure A.1(a) the minimum r is 0.053. With this value the two-norm of the expression in (A.2) can be obtained as shown in Figure A.1(b). From Figure A.1(b) it can be seen that the two-norm of the expression in Equation (A.2) is always smaller than 0.5. Therefore, the convergence can be guaranteed if choose the initial point as $x^0 = [0, \frac{T_e^{\text{ref}}}{1.5p\psi_f}]^T$.

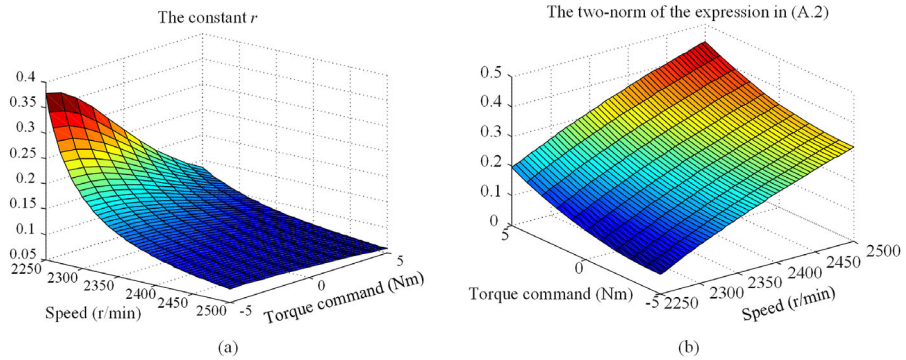

FIGURE A.1 (a) The minimum constant r with respect to different speed and torque in the CPOM2; (b) The two-norm of the expression in (A.2) at different speed and torque